The International Journal of Advanced Manufacturing Technology
https://doi.org/10.1007/s00170-024-13526-7

ORIGINAL ARTICLE

Impact of process parameters on the dynamic behavior of Inconel 718 fabricated via laser powder bed fusion

Michele Abruzzo[1] · Giuseppe Macoretta[1] · Bernardo Disma Monelli[1] · Luca Romoli[1]

Received: 19 January 2024 / Accepted: 23 March 2024

Abstract
In this research, we investigate the dynamic behavior of Inconel 718 fabricated through laser powder bed fusion (L-PBF), addressing a notable knowledge gap regarding the correlation between process parameters and dynamic properties. The process parameters adopted are deducted from an extension of the Rosenthal solution, formulated to increase the process productivity while avoiding the typical production process defects. The dynamic Young modulus and the structural damping of the material are estimated as a function of the process parameters through ping tests reproducing the flexural vibrations of the specimens in as-built, solutioned, and aged conditions. The microstructure and porosity are investigated through metallographic analyses. The results show a substantial influence of the L-PBF process parameters on the dynamic Young modulus, which markedly increases as the energy density is reduced (23%) and progressively becomes more similar to the conventionally produced material. This influence stands in stark contrast to the relatively modest impact of heat treatments, which underlines a negligible effect of the process-induced residual stress. The structural damping remained approximately constant across all test conditions. The elastic response of the material is found to be primarily influenced by the different microstructures produced as the L-PBF process parameters varied, particularly in terms of the dimensions and shape of the solidification structures. The unexpected relationship between the dynamic Young modulus, energy density, and microstructure unveils the potential to fine-tune the material's dynamic behavior by manipulating the process parameters, thereby carrying substantial implications for all the applications of additively manufactured components susceptible to significant vibratory phenomena.

Keywords Laser powder bed fusion · Nickel-based alloys · Ping testing · Metallographic analysis · Dynamic behavior

1 Introduction

The extension of rapid prototyping to metallic materials through processes such as laser powder bed fusion (L-PBF), electron beam melting (EBM), and direct energy deposition (DED) has resulted in a significant increase in the usage of additively manufactured components in several industrial applications [1, 2]. As some examples [3], stainless steel is widely used in the food industry due to its high mechanical strength and corrosion resistance. High-strength titanium alloys lend themselves well to creating complex shapes for bone or tissue prostheses in the biomedical industry. Aluminum alloys are employed in the aerospace industry to produce thin-walled and lightweight parts with complex geometries. Nickel-based superalloys, such as Inconel 718, are adopted to realize turbochargers, nuclear reactors, gas turbines, airplane parts, and all those mechanical components which require high mechanical performances at high temperatures. Inconel 718 and 625 are also extensively employed at room temperature in the oil and gas and chemical industry for the production of valves and critical components due to their utmost resistance to corrosion and hydrogen embrittlement, associated with their high static and cyclic strength [4, 5]. Modern additive manufacturing techniques allow the pro-

All authors contributed equally to this work.

✉ Michele Abruzzo
michele.abruzzo@ing.unipi.it

✉ Giuseppe Macoretta
giuseppe.macoretta@unipi.it

Bernardo Disma Monelli
bernardo.disma.monelli@unipi.it

Luca Romoli
luca.romoli@unipi.it

[1] Dipartimento di Ingegneria Civile e Industriale, Università di Pisa, Largo Lucio Lazzarino 2, Pisa 56122, Toscana, Italia

Published online: 15 April 2024

duction of mechanical components characterized by complex geometries, which may not be obtainable through standard manufacturing techniques (as in the case of lattice structures [6–13]). In addition, the mechanical performances of additively manufactured components are comparable or superior to the analog obtained through traditional processes [14]. Given the interaction between several physical phenomena, the qualification of additive manufacturing processes is more complex than traditional ones. Moreover, it involves materials, process parameters, and heat treatments, which are the subject of several recent research works.

Several studies [15–22] characterized the influence of the process parameters adopted during the printing process on the bulk (Young modulus, yield and tensile strength, ductility, elongation at break, porosity) and surface (fatigue strength, surface roughness) properties of the material. Considering the widely used L-PBF process, the features of the metal powder used, the parameters of the laser beam, and the heat treatments undergone by the material are the most influencing factors for the final properties of the printed component [23–27]. Adopting a different scanning strategy, printing direction, layer thickness, hatch distance, and energy density produces different surface textures, microstructures, and mechanical properties of the material [28–37]. Liu et al. [38] investigated the effect of energy density on the texture and mechanical anisotropy in selective laser-melted Inconel 718. They demonstrated that a high energy density increases the anisotropy in the yield strength of the material, while lower energy densities correspond to finer microstructures. Wu [39] investigated the effects of energy density on the formation of metallurgical defects. Zhang et al. [40] studied three different scanning strategies to modify the surface finish and microstructure of selective laser-melted specimens maximizing their wear resistance. Simonelli [41] and Bertolini [42] analyzed the effects of printing direction on the mechanical properties and anisotropic behavior of different printed materials. Other studies characterized the fatigue resistance and the propagation of cracks as a function of the process parameters [43, 44] and the build orientation [45–47].

The high heat input of the laser beam produces severe thermal cycles in most of the additive processes with metal powders, generating high residual thermal stresses [48–50] that are usually reduced or removed through heat treatments [51] or different scanning strategies [52]. Tucho et al. [53] studied the dissolution of macro- and micro-segregated precipitates in Inconel 718 specimens obtained by L-PBF by varying the temperature and the total time of the heat treatment. Shin et al. [54] studied the evolution of the microstructure and mechanical properties of stainless steel 316L prepared via L-PBF for several heat treatments. All those studies demonstrated that residual stresses influence the mechanical properties of the printed component, but their effects can be limited through different heat treatments. Furthermore, heat treatments can be adopted to enhance the material's properties and modify its microstructure.

In many industrial applications, such as in the turbomachinery or aerospace industry, additively manufactured components can experience vibrations of different magnitudes, making the identification of the dynamic properties of the material mandatory. The dynamic Young modulus and the structural damping of components obtained through standard manufacturing processes have been extensively studied [55, 56]. On the contrary, investigations on the dynamic behavior of additively manufactured components are still limited. Maconachie [57] and Carassuss [58] characterized the influence of the strain rate on the mechanical properties of specimens obtained by L-PBF with different building orientations and thicknesses. Ge et al. [59] studied the behavior of selective laser-melted 316L stainless steel produced at different scanning speeds, identifying constitutive models of the material as a function of the strain rate and the process parameters employed. Scalzo et al. [60] used different experimental setups to quantify the dissipative properties of L-PBF lattice structures. Furthermore, the material's microstructure constitutes a critical element for the mechanical properties of additively manufactured components, but only its influence on the static properties of the material (bulk or surface) has been extensively studied.

The literature review carried out emphasizes the need for further research on the dynamic behavior of additively manufactured materials, which is particularly concerning given the increasing usage of additive manufacturing in applications ranging from aerospace parts to biomedical implants, where components are frequently subject to dynamic forces and vibrations. While some previous studies have begun to characterize the influence of the strain rate on these materials, the broader dynamic behavior still remains inadequately explored. Moreover, the influence of key factors such as process parameters and heat treatments on the dynamic properties (dynamic Young modulus and structural damping) of additively manufactured components is still unclear. The limited research in this domain hampers our ability to optimize the process and predict the behavior of additively manufactured parts in frequency-dependant scenarios, leaving a significant knowledge gap that needs to be addressed to ensure reliable and safe applications.

In this context, the present study introduces a novel systematic methodology to comprehensively characterize the dynamic behavior of additively manufactured metals as a function of the process parameters employed, focusing on Inconel 718 specimens fabricated through laser powder bed fusion (L-PBF). The dynamic Young modulus and the structural damping of the material were obtained for eight different combinations of the process parameters derived from an extension of the Rosenthal solution. The proposed formulation was used to increase the process productivity

while avoiding the typical defects of the L-PBF process (i.e., lack of fusion, meltpool instability, and keyhole). The specimens were characterized through a series of ping tests carried out on a test rig reproducing free vibrations according to the first bending mode, which is notoriously the most important for the quantification of the energy dissipation of the material. Moreover, the material was tested in three distinct conditions: as-built, solutioned, and aged. The three material conditions tested were used to highlight the influence of the process parameters taken alone, the influence of any residual stress resulting from the printing process, and the effect of the material's strengthening through the precipitation of intermetallic compounds. The porosity and microstructural features were studied as a function of the process parameters using a series of metallographic assessments and subsequently correlated to the dynamic properties of the material.

2 Specimen manufacturing

The specimens were produced in the "Metal Additive Manufacturing" laboratory of the University of Pisa using a Renishaw RenAM 500 S Flex L-PBF machine. The machine can operate in continuous or pulsed wave laser emission, and a maximum output power of 500 W can be produced. The material used is a standard Inconel 718 powder supplied by Heraeus Additive Manufacturing GmbH, compliant with the ASTM F3055 standard. The particle size distribution is comprised between 13 and 53 μm (D10 ÷ D90).

The specimens were produced in a single batch and with the same vertical building direction to exclude the effect of the building orientation on the material's dynamic properties (Fig. 1). The hatching region was obtained using a stripe scanning pattern with layers rotated by 67°. A continuous wave emission of the laser beam was employed. During the printing process, the built plate was preheated to 170 °C to minimize the residual stresses. The process chamber was filled with argon gas, reaching an oxygen concentration lower than 7 ppmw.

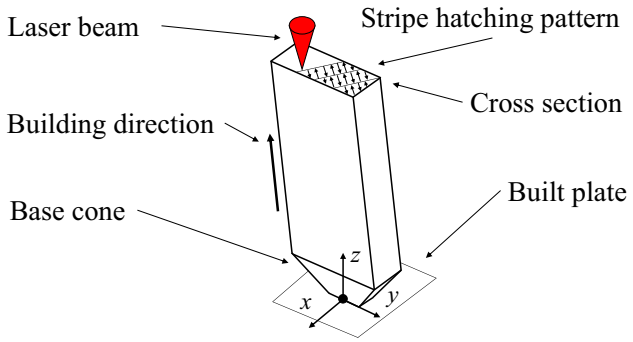

Fig. 1 Specimen building strategy

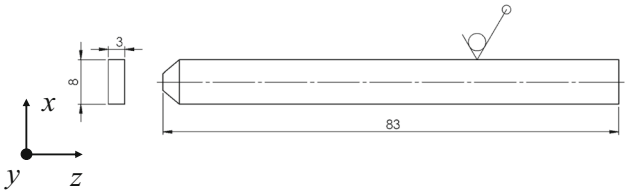

Fig. 2 Specimen geometry and dimensions (reported in mm)

The geometry of the specimens is reported in Fig. 2. The specimens were designed for the ping tests, featuring a rectangular cross-section to simplify the application of an impulsive excitation on their larger flat side. The ratio between the characteristic dimension of the cross-section and the specimen's length is equal to 10. The specimen's dimensions were chosen to maximize the built plate usage, thus reducing the powder waste. The region of connection with the built plate is a truncated pyramid, sized to simplify the detachment and extraction of the specimens.

The material was investigated in the as-built, solutioned, and aged conditions. Following the execution of the ping tests in the as-built condition, the same specimens were subjected to a solutioning heat treatment (980 °C for 1 h, followed by furnace cool until room temperature). Again, after the execution of the ping tests in the solutioned conditions, the specimens were subjected to an aging heat treatment (720 °C for 8 h, furnace cooling until 650 °C at 55 °C/h followed by 8 h at 650 °C, and a final furnace cooling until room temperature). Both heat treatments were carried out in a Nabertherm LH/120 furnace using a protective atmosphere with argon gas to minimize the formation of surface oxides.

2.1 Process parameters selection

The process parameters used to print the specimens were chosen on the basis of an extension of the Rosenthal solution [40, 61, 62], which describes the thermal field produced in L-PBF processes. The formulation, proposed by Moda [25], was validated by Macoretta et al. [44], who demonstrated that process parameters belonging to the so-defined L-PBF feasible region produce a material not affected by macroscopic metallurgical defects, and having only a slight reduction in the fatigue strength. The adopted formulation correlates the main process parameters (laser power, scan speed, hatch distance, layer thickness) and the material thermal properties through two dimensionless parameters, namely the normalized speed V^* and power P^*. The main result of this formulation is the process feasible region, which defines all the combinations of process parameters that guarantee the absence of typical metallurgical defects, such as lack of fusion (LoF), meltpool instability, or keyhole.

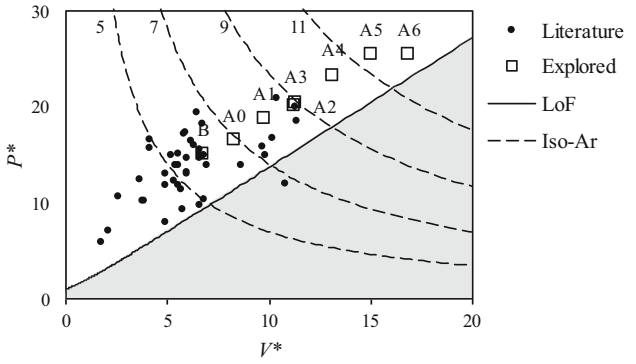

Fig. 3 L-PBF process feasible region (white hatched region). Literature data and A_2, A_3, and A_5 are obtained from [25, 44]

The final process parameter combinations adopted in the present work are an extension of those used in [44] and were determined starting from the baseline values suggested by Renishaw and already investigated in other studies [37, 43] (hereafter defined as *Baseline*). The remaining combinations were obtained within the feasible region by moving along a straight line having a similar margin with respect to the lack of fusion (LoF) region (hereafter defined as A_i). The proposed logic determines the process parameters within the feasible region by progressively reducing the energy density and increasing the process productivity, obtaining significant advantages from an industrial point of view. The total number of configurations adopted was equal to 8 (Fig. 3), and four specimens were printed and tested for each combination of parameters to give statistical relevance to the collected data. All the parameters employed are reported in Table 1, in which P is the laser beam power, v the scan speed, h the hatch distance, t the layer thickness, A_r the aspect ratio of the molten pool, E_d the volumetric energy density, and B_r the process build rate. For each combination of parameters, the build rate B_r was calculated as the printed volume per unit of time:

$$B_r = thv$$

and the volumetric energy density E_d, used to represent the integral effect of all the process parameters, was calculated as the ratio between laser beam power and the process build rate:

$$E_d = \frac{P}{thv}$$

The layer thickness and the hatch distance were kept constant for all the combinations of the parameters except for the A_3 specimens, which were printed with a higher hatch distance. The safety margin was slightly reduced for the A_6 specimens, which were obtained by increasing the scan speed at the same power as the A_5 configuration. It can be noticed that, at the lowest energy density, the process build rate can reach a 150% increase compared to the *Baseline* case. Compared to [44], which adopted only the A_2, A_3, and A_5 parameters, the higher number of combinations adopted allows to analyze in detail the effect of the process parameters on the dynamic properties of the material.

2.2 Dimensional analysis of the specimens

The specimens were visually inspected to verify the absence of thermal distortions. It was verified that, regardless of the process parameters adopted, the specimens are not affected by any permanent deformation related to the printing process.

All the specimens were subject to an accurate dimensional analysis to verify the correspondence of the actual geometry with the nominal one. The dimensions of each specimen's section (w and s) were measured at five longitudinal positions using a blade micrometer, having an accuracy of 0.01 mm. Given the reduced blade thickness (0.7 mm), the micrometer measures the specimen's dimensions avoiding any effect related to the maximum height of the roughness peaks [44] (i.e., residual powder inclusions or surface defects), which would produce an overestimation of the specimen's section and an underestimation of the dynamic Young modulus of the material. The length of the truncated pyramid L_c and the specimen's total length L were measured using a centesimal

Table 1 L-PBF process parameters, melt pool aspect ratio, energy density, and build rate

	P (W)	v (m/s)	h (μm)	t (μm)	A_r (-)	E_d (J/mm^3)	B_r (mm^3/s)
Baseline	280	0.90	90	60	6	57.6	4.9
A_0	310	1.10	90	60	7	51.9	5.9
A_1	350	1.30	90	60	8	49.9	7
A_2	375	1.50	90	60	9	46.3	7.8
A_3	460	1.50	135	60	9	45.4	10.1
A_4	435	1.75	90	60	10	46.0	9.5
A_5	475	2.00	90	60	11	44.0	10.8
A_6	475	2.25	90	60	12	39.1	12.2

Table 2 Dimensional analysis results

	L (mm)	L_c (mm)	w (mm)	s (mm)	m (g)
Baseline	83.02 ± 0.42	3.12 ± 0.01	8.02 ± 0.01	3.04 ± 0.01	16.57 ± 0.01
A_0	83.00 ± 0.42	3.12 ± 0.02	8.03 ± 0.02	3.05 ± 0.04	16.55 ± 0.01
A_1	83.03 ± 0.41	3.11 ± 0.01	8.02 ± 0.01	3.03 ± 0.01	16.54 ± 0.01
A_2	83.03 ± 0.42	3.25 ± 0.02	8.04 ± 0.01	3.03 ± 0.01	16.43 ± 0.01
A_3	83.06 ± 0.42	3.10 ± 0.02	8.05 ± 0.01	3.04 ± 0.01	16.91 ± 0.01
A_4	83.19 ± 0.42	2.91 ± 0.01	8.02 ± 0.01	3.02 ± 0.02	16.37 ± 0.01
A_5	83.14 ± 0.42	2.93 ± 0.02	8.03 ± 0.01	3.01 ± 0.01	16.27 ± 0.01
A_6	83.12 ± 0.42	3.12 ± 0.02	8.02 ± 0.02	3.01 ± 0.01	16.22 ± 0.01

caliper. The mass m was measured using a high-precision scale.

The results of the dimensional analysis are reported as the mean value and standard deviation of each specimen's dimension in Table 2. All the dimensions are not affected by significant dependencies on the process parameters adopted, the measured dispersion is limited, and the differences from the nominal dimensions are lower than 1%. The maximum difference from the nominal dimensions is obtained on the length of the truncated pyramid, which is highly dependent on the specimen's removal from the building plate and is in the order of 2%.

Finally, the material's mass density ρ was calculated as the ratio between the measured mass and the volume of each specimen calculated using its mean dimensions. The average material mass density is the same as Inconel 718 obtained through traditional manufacturing processes and is equal to $\rho = 8300 \pm 15 \text{kg/m}^3$.

3 Experimental tests and numerical methods

3.1 Ping test setup

A series of ping tests were used to characterize the dynamic properties of the specimens obtained by L-PBF. Following the ASTM E1876-21 standard [63], the ping test consists of the application of an impulsive excitation to the specimen through an impact tool (which can be instrumented or not) and in the measurement of the subsequent dynamic response. The specimen can vibrate freely according to its natural modes, eliminating the need for complex support systems, elaborate setups, or alignments. The spectral analysis of the specimen's response and the study of the related frequency response function (FRF) allow the quantification of the natural frequencies of the stimulated natural modes and to derive, through analytical or finite element models, the dynamic Young modulus of the material E and the associated structural damping ζ. Any spurious frequency component can be easily filtered, and the test typically features high repeatability. Compared to standard tests, ping tests allow simple, rapid, and accurate characterizations of the dynamic properties of the material obtained by additive manufacturing without the need for any preliminary preparation of the specimens.

In the present study, the ping tests were performed using the equipment shown in Fig. 4. The impulsive excitation was applied through a Dytran 5800SL impulse hammer. The dynamic response was measured using a Polytec OFV 551 laser optic-fiber vibrometer featuring a maximum sampling rate of 50 kHz. The specimen was instrumented using a reflective stamp and was supported by two cylindrical pins (3 mm diameter) placed on L-shaped supports, which can slide along horizontal guides to allow the testing of specimens with different dimensions. The pins were located on the nodes of the first bending mode, whose position depends solely on the specimen's geometry (Fig. 2). For the specimens considered, the first node is located at 18.3 mm from the flat end of the specimen, and the distance between the nodes is equal to 45 mm. The impulsive excitation and the dynamic response (speed acquisition) were applied/measured on the anti-nodal position (i.e., in correspondence with the specimen's center). In the adopted test configuration, the specimen vibrates in

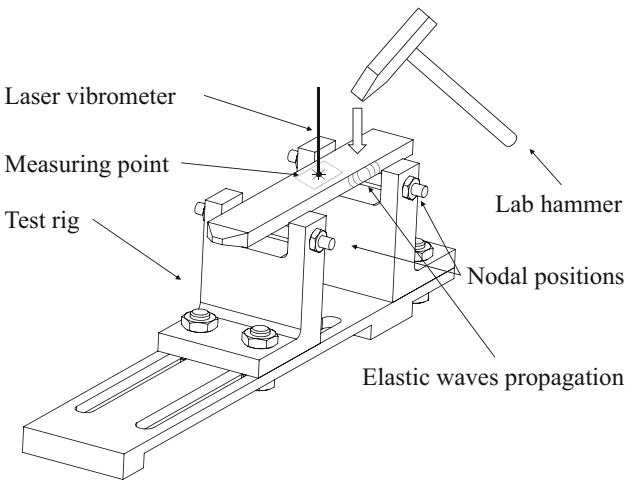

Fig. 4 Ping test scheme and test rig setup

free-free conditions according only to its first bending mode, eliminating any dissipative contribution associated with the test rig and allowing the measurement of the structural damping of the material. The test was repeated five times for each specimen. Considering that four specimens were printed for each process parameters combination and that three material conditions were considered, a total of 480 tests were executed. In addition, a conventional hot-rolled Inconel 718 rod was tested to obtain a reference value of the dynamic Young modulus. The rod has a diameter of 15.92 mm and a length of 475 mm and was tested in the solutioned and aged material condition.

3.2 Dynamic Young modulus calculation

The dynamic response of the specimens was processed through a fast Fourier transform (FFT) to determine the frequency of the first bending mode f_r, which can be directly correlated to the dynamic Young modulus of the material E.

The dynamic Young modulus was identified using an accurate 3D finite element model (FEM) that was set up and solved using the ANSYS mechanical modal analysis environment. The dimensional analysis results (Sect. 2.2) show that the specimen's geometry is identical to the nominal one. Therefore, as no geometry-related effect will be present when calculating the material's dynamic properties, the model reproduced the nominal geometry of the specimens. The material was assumed to be linearly elastic, homogeneous, and isotropic, using the measured density and Poisson's ratio of the conventional Inconel 718 ($\nu = 0.294$) as fixed inputs. The proposed model neglects the effects of the material porosity and well-known anisotropic behavior due to the building direction of the L-PBF process. The former can be assumed having a limited effect when evaluating a bulk property such as the dynamic Young modulus, especially in cases where high material density is expected. The latter should not affect the evaluation of the dynamic Young modulus in the z direction. The mesh was made of 8 nodes brick elements. The final element size was determined based on a convergence analysis made on the frequency of the first bending mode, which coincides with the natural mode measured experimentally (Fig. 5). On average, the total number of nodes and elements was equal to 7500 and 1300, respectively.

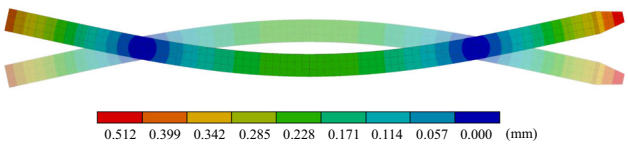

Fig. 5 Finite element model modal shape of the first bending mode

As the specimen was modeled without constraints, the finite element model reproduced the free-free experimental testing conditions. Given the model's linearity, the dynamic Young modulus of the material was modified until the simulated frequency of the first bending mode was equal to that measured experimentally for each specimen in each testing condition.

3.3 Structural damping calculation

The structural damping of the material was calculated from the dynamic response of the specimen. The experimental signal was filtered using a band-pass filter having a bandwidth equal to [f_r-100, f_r+100] Hz, which eliminates any spurious component present in the dynamic response of the system (i.e., test rig, electrical or measurement noise) and isolates the free oscillation according to the specimen's first bending mode. The damping ratio of the material was then calculated using the logarithmic decrement method, filtered through a 10-value moving average. The specimen's response was approximated with a one degree-of-freedom damped harmonic oscillator having imposed an initial speed:

$$\dot{x}(t) = \dot{x}_{\text{in}} e^{-\zeta 2\pi f_r T} \cos(2\pi f_r T)$$

in which $\dot{x}$ is the instantaneous speed of the measured point, $\dot{x}_{\text{in}}$ is the initial speed, T is the time, and ζ is the calculated material's damping ratio. As shown in Fig. 6, the theoretical response obtained through the proposed methodology reproduces the experimental one with high accuracy.

3.4 Microstructural analysis

The material's microstructure was analyzed by means of low-magnification optical microscopy. After the execution of the ping tests, samples were obtained from each aged specimen along the longitudinal and transversal directions, namely parallel and orthogonal to the specimen build direction. The samples were prepared following the standard metallographic procedure (ASTM E3-11 standard) and etched using Kalling's II (n.94, ASTM E407) reagent. The mirror-polished samples were observed before and after the chemical etching. The software ImageJ [64] was used to calculate the material density d and to analyze the pore size, shape, and distribution as a function of the process parameters adopted. At least ten samples extracted on each direction were investigated per each process parameters set. The samples were extracted at different positions along the specimen's length to highlight any potential microstructural heterogeneity along the build direction [65, 66].

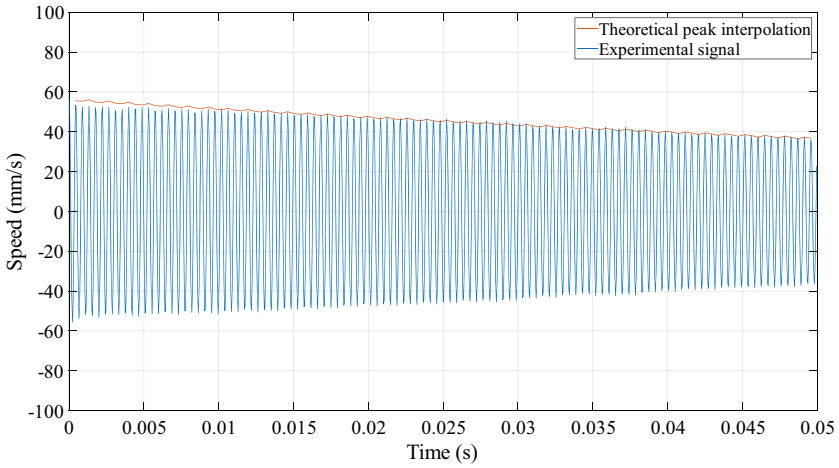

Fig. 6 Comparison between the experimental signal and the theoretical response of the one degree-of-freedom oscillator (A_2 parameters)

4 Results

4.1 Dynamic behavior

As shown in Fig. 7, the dynamic Young modulus E of the material is highly dependent on the process parameters adopted regardless of the heat treatment undergone by the specimens. In fact, by condensing the effect of the process parameters in the energy density, E decreases with the E_d following an approximately parabolic trend that remains unchanged following the solutioning and aging heat treatments. In the as-built conditions, E has a maximum increase of 23% compared to the *Baseline* parameters, reaching a plateau for $E_d = 45.4$ J/mm^3. At lower energy densities ($E_d < 45.4$ J/mm^3), it undergoes negligible variations (less than 1.5%) and remains approximately constant. The solutioning treatment translates the curves upwards and produces an average increase of E equal to 3.4%. The same considerations are valid for the aging treatment, which causes an average increase of E of 5.5% compared to the as-built conditions and 1.5% compared to the solutioned specimens. For each energy density, E shows limited standard deviations (Table 3), implicating high repeatability of the technological process. The specimens obtained at lower energy density show a reduced dispersion of E, while the values of E obtained with the *Baseline* parameters are affected by high variability, with a maximum variation equal to approximately 6% of the mean value. All the tests performed on a single specimen returned the same natural frequency, indicating that the dynamic Young modulus dispersion depends on the L-PBF process rather than the measurement method. After the heat treatments, the deviation of the dynamic Young modulus remains contained and undergoes a modest reduction for all the process parameter sets.

The dynamic Young modulus obtained for the conventional Inconel 718 bar was 209 GPa, in line with the literature results [67]. From the comparison with the results of the ping tests, it emerges that the material obtained by L-PBF has a dynamic behavior that is more similar to the conventional one for lower values of energy density (Fig. 7). The dynamic Young modulus obtained for the conventional Inconel 718

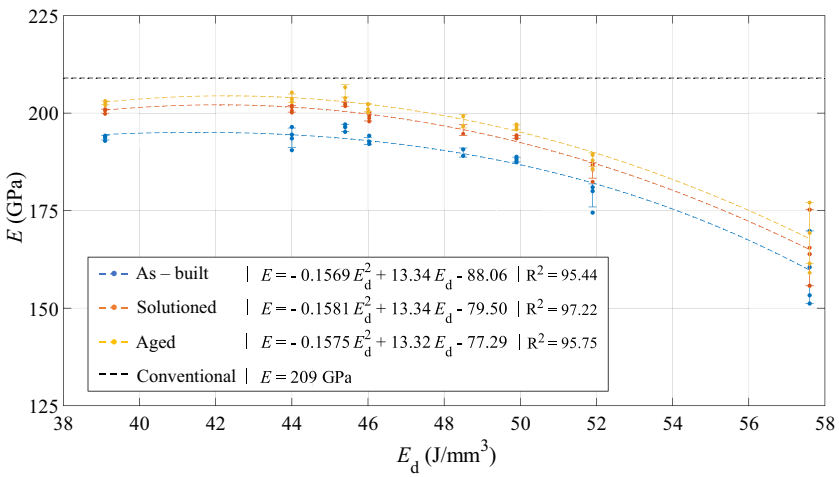

Fig. 7 Dynamic Young modulus obtained as a function of the energy density for several heat treatments. The parabolic regressions of the average values and the results of the conventional Inconel 718 rod are represented with a dashed line

Table 3 Dynamic Young modulus obtained as a function of the energy density for several heat treatments

E (GPa)	As-built	Solutioned	Aged
Baseline	160.5 ± 9.3	165.5 ± 8.5	169.3 ± 7.8
A_0	178.9 ± 2.9	185.3 ± 2.0	188.1 ± 1.8
A_1	188.1 ± 0.6	193.9 ± 0.4	196.4 ± 0.6
A_2	189.9 ± 1.2	195.7 ± 1.4	197.9 ± 1.7
A_3	192.9 ± 0.9	199.0 ± 1.0	201.4 ± 1.0
A_4	196.2 ± 0.9	202.3 ± 0.5	205.7 ± 1.6
A_5	193.7 ± 2.5	201.1 ± 0.8	203.8 ± 1.0
A_6	193.7 ± 0.6	200.5 ± 0.5	202.7 ± 0.5

Table 4 Damping ratio obtained for several combinations of process parameters and heat treatments

ζ (‰)	As-built	Solutioned	Aged
Baseline	0.46 ± 0.14	0.47 ± 0.14	1.01 ± 0.32
A_0	0.84 ± 0.43	1.60 ± 0.65	1.37 ± 0.31
A_1	1.26 ± 0.91	0.80 ± 0.19	1.09 ± 0.21
A_2	0.91 ± 0.18	0.39 ± 0.11	0.97 ± 0.39
A_3	1.06 ± 0.49	0.76 ± 0.24	0.91 ± 0.25
A_4	0.61 ± 0.07	1.26 ± 0.22	1.47 ± 0.32
A_5	1.16 ± 0.23	1.05 ± 0.49	1.44 ± 0.42
A_6	0.89 ± 0.34	0.94 ± 0.21	1.15 ± 0.11

can be considered a limit process value, with a minimum difference of 1.6% (obtained for $E_d = 46$ J/mm^3).

The structural damping associated with the material does not vary significantly with the energy density and is approximately constant for the different combinations of process parameters (Fig. 8). Moreover, the heat treatments were found not to modify the damping ratio. As reported in Table 4, the average value of the damping ratio is equal to 0.0009 regardless of the process parameters or material condition considered. The standard deviation is high and reaches a maximum variation of 60% compared to the mean value (as-built A_1). As an evanescent quantity is evaluated, micro-sliding phenomena can significantly influence the test result. Nonetheless, the tests carried out are fundamental for the dynamic applications of the material as they highlight the independence of this characteristic property from the production process and any heat treatments.

4.2 Material's microstructure

The material porosity was calculated as a function of the process parameters using the mirror-polished specimens, observed at 2.5× magnification. Four metallographies obtained for different combinations of the process parameters are reported in Fig. 9. As can be observed in Fig. 9a, the *Baseline* parameters produce a full-dense material ($d = 99.99 \pm 0.01$ %). The only pores present are due to the typical gas-entrapped bubbles, which are easily recognizable by their perfectly round shape and limited size (approximately 10 μm diameter). By reducing the energy density (i.e., increasing the scan speed and the laser power), the molten pool becomes progressively more elongated and thus prone to humping instability [25, 68], and the pores assume the characteristic comma shape while increasing in size [69]. These phenomena are enhanced for the lowest energy density values, as can be observed by taking the A_6 specimen as an example (Fig. 9d). Quantitatively, all the process parameters combinations adopted, except for the process parameters A_3 and A_6, produce a full-dense material characterized by a material density featuring a mean value of about 99.98% and a low standard deviation (Table 5). For the A_3 specimens, increasing the hatch distance favors the occurrence of LoF phenomena, especially in the sub-superficial regions, probably due to meltpool instabilities. On the other hand, the lower material density of the A_6 specimens is attributable to the reduced safety margin adopted with respect to the LoF

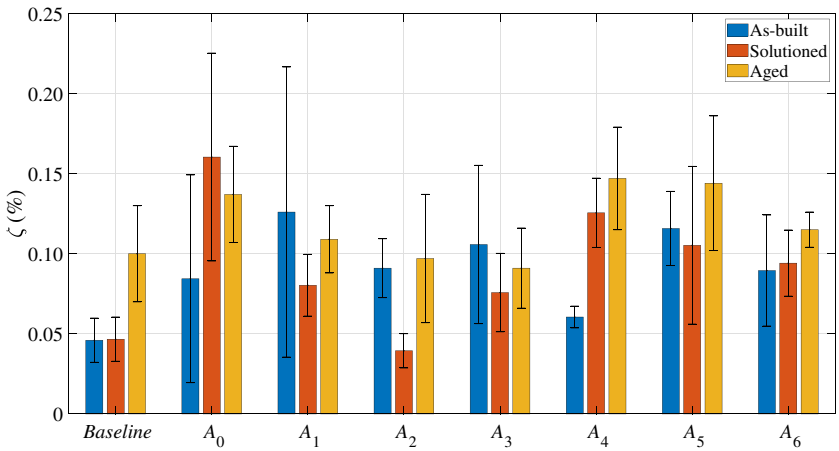

Fig. 8 Damping ratio obtained for several combinations of process parameters and heat treatments

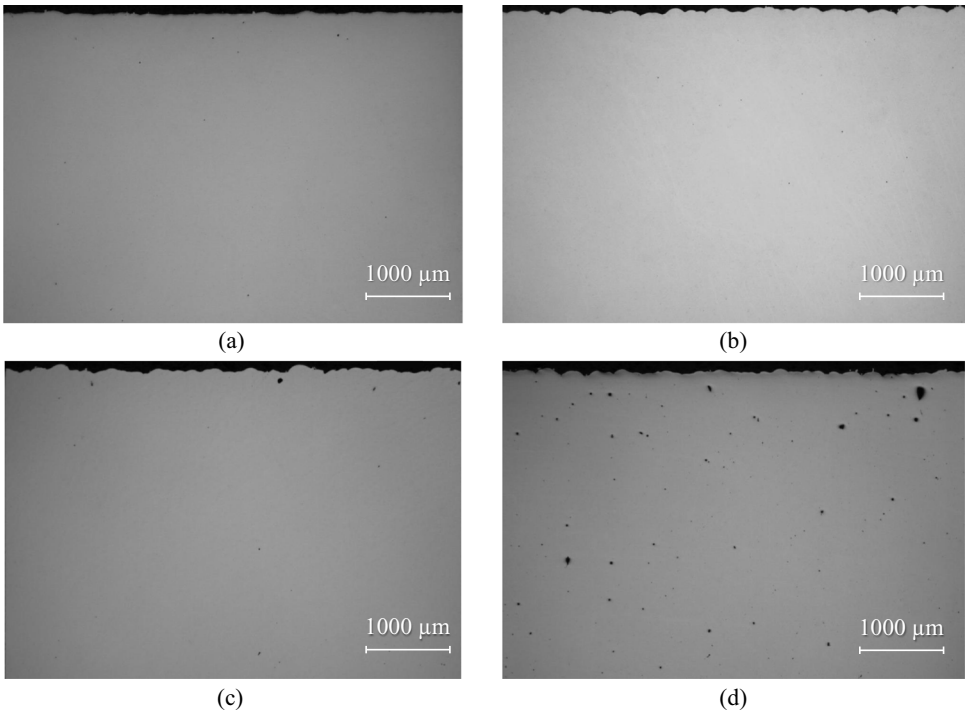

Fig. 9 Longitudinal sections obtained through low-magnification optical microscopy (2.5×) after mirror polishing the specimen's samples for several combinations of the process parameters. **a** *Baseline*. **b** A_1. **c** A_4. **d** A_6

region, which is produced by increasing the scan speed without increasing the laser power (compared to the A_5 process parameters). The feasible region adopted is thus experimentally validated, up to build rate values that are more than double the *Baseline* value.

The evolution of the material's microstructure is represented in Fig. 10 for four combinations of the process parameters (10× magnification). The microstructure obtained with the *Baseline* parameters (i.e., with the highest energy density) is characterized by several columnar structures (Fig. 10a), which are mainly parallel, oriented along the build direction (longitudinal direction of the specimen), and extended across several layers. The molten pools are easily distinguishable due to precipitates that pile up at their boundary. On average, the columnar structures extend through 20 layers. By reducing the energy density, the material's microstructure undergoes a gradual change, mainly involving the features of the solidification structures (Fig. 10b, c, and d). By simultaneously increasing the laser power and scan speed, the adopted process parameter sets increase the meltpool aspect ratio and reduce the specific heat input (proportional to the volumetric energy density). The meltpool cooling rate is thus increased, producing more severe thermal cycles. Compared to the *Baseline* parameters, randomly oriented dendritic structures with limited elongation can be observed (Fig. 10d), hinting at the occurrence of complex three-dimensional cooling thermal gradients, which locally overcome the global one aligned with the build direction. The higher cooling rate considerably reduces the longitudinal extension of the typical L-PBF dendritic structures and produces a finer grain [33]. The microstructure's evolution is coherent with the super-cooling theory [70, 71], according to which the cooling structures are oriented as the cooling thermal gradient (main solidification direction) and have an extension inversely proportional to the cooling rate of the molten material. Excluding the base cone, where thermal gradient and cross-section variations may result in microstructural differences, the microstructure appears homogeneous and continuous along the build direction and shows no significant variations. Moreover, the dynamic properties of the specimen predominantly rely on the microstructure of the majority of the material volume involved in the test, and any minor variation in the microstructure would produce a negligible effect on the test results [63, 72].

Table 5 Material density obtained as a function of the process parameters considering both longitudinal and transverse sections

	d (%)
Baseline	99.99 ± 0.01
A_1	99.99 ± 0.01
A_2	99.99 ± 0.01
A_3	99.92 ± 0.10
A_4	99.98 ± 0.01
A_5	99.96 ± 0.02
A_6	99.89 ± 0.06

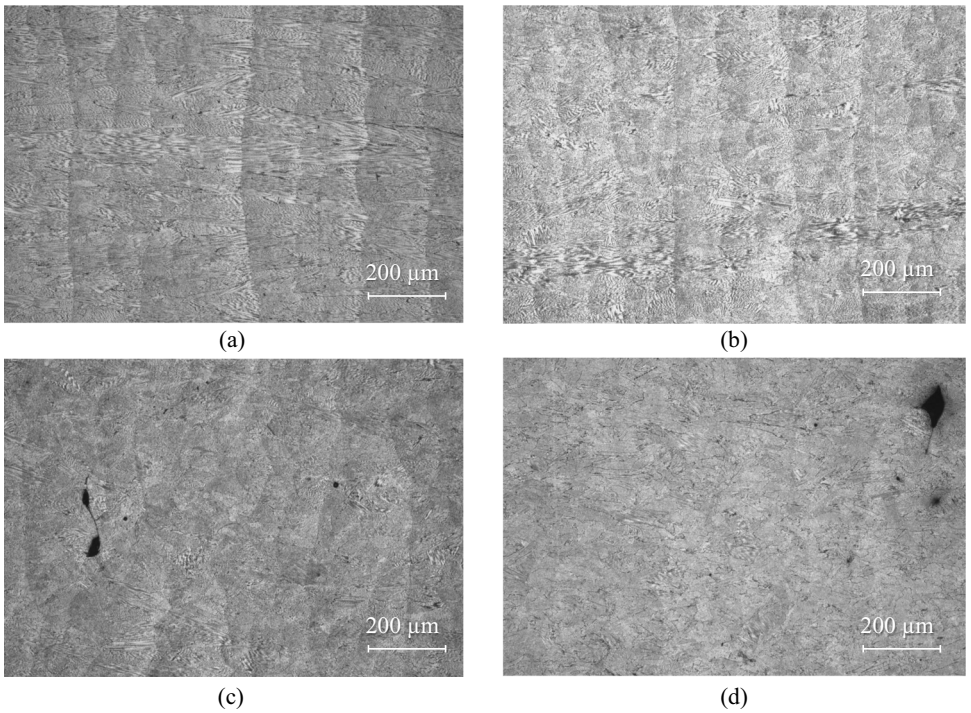

Fig. 10 Material's microstructure obtained through low-magnification optical microscopy (10×) for several combinations of the process parameters, etchant Kalling's II. **a** *Baseline*. **b** A_1. **c** A_4. **d** A_6

5 Discussion

The results show a close correlation between the dynamic properties of the Inconel 718 obtained by L-PBF and the process parameters adopted. The ping tests highlighted a marked dependency of the specimen's natural frequencies on the energy density. At the same time, the structural damping associated with the material was not significantly affected. In general, fixing a mechanical component's geometry, mass density, and stiffness determines its natural frequencies uniquely: this means that the three main influencing factors to be analyzed to explain the different dynamic behavior are the specimens' dimensions and mass density and dynamic Young modulus of the material, which is, in turn, a function of the elastic wave propagation in the microstructure.

As discussed in Sect. 2.2, the specimens did not present any thermal distortions after the printing process or the heat treatments due to the vertical build direction. The specimen's dimensions were measured using a blade micrometer and a centesimal caliper for its transverse and longitudinal directions, respectively. The average section dimensions resulted to be not influenced by the adopted printing parameters and not significantly different from the nominal ones (differences lower than 1%). The process parameter variations produce different surface roughness profiles, depending on the stability of the molten pool, and the pitch between the roughness peaks increases with the energy density (Fig. 11). However, the blade micrometer produces a more accurate estimate of the specimen's local dimensions, purging the measurement of the more irregular roughness peaks, which would be irrelevant to the dynamic behavior. A sensitivity analysis to the effects of the specimen dimensions was done by including the geometry variations in the finite element model: the minimum (maximum) value of the dynamic Young's modulus is obtained by considering the longest (shortest) specimen and the smallest (largest) cross-section. Moreover, considering $L = 83.45$ mm, $L_c = 3.25$ mm, $w = 8.05$ mm, and $s = 3.05$ mm, the difference with the dynamic Young

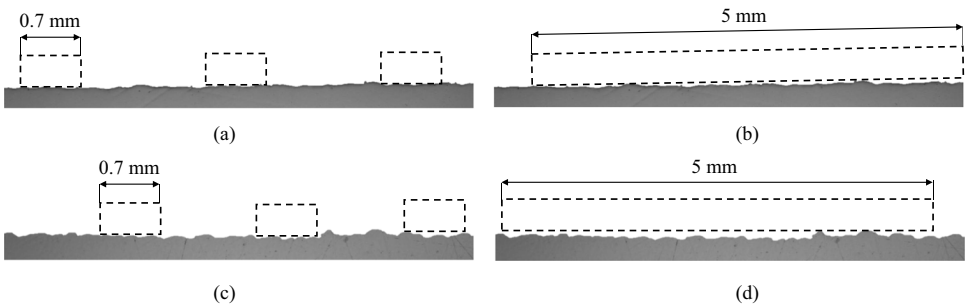

Fig. 11 Measurement of the specimen section using a blade (**a**, **c**) and a standard micrometer (**b**, **d**) for two combinations of process parameters. **a**, **b** *Baseline* process parameters. **c**, **d** A_5 process parameters

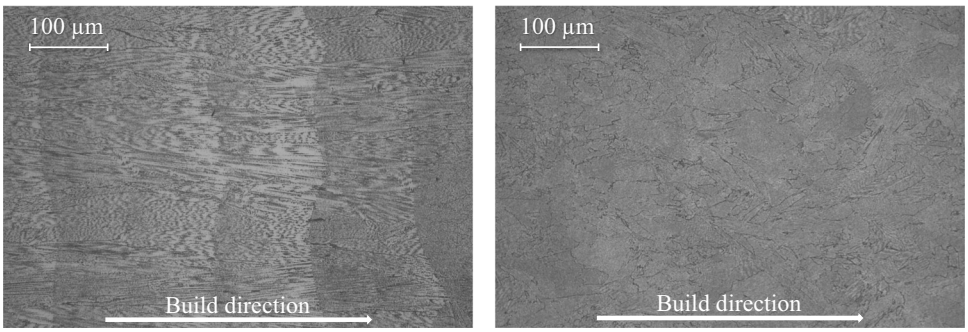

Fig. 12 Material's microstructure obtained through low-magnification optical microscopy (20×), comparison between the *Baseline* (**a**) and A_6 (**b**) process parameters

modulus obtained using the nominal geometry is only 4 GPa (lower than 3%). The geometry variations induced by the process parameter sets are not enough to justify the different dynamic behavior.

The mass density of the L-PBF-produced specimens is similar to that of the Inconel 718 obtained through traditional processes. The porosity is lower than 0.11% for all the process parameter combinations (Table 5). Its effects were evaluated by introducing the minimum material density (d=99.89%) in the finite element model, with nominal specimen dimensions. It yields a dynamic Young modulus which differs by 0.06% compared to that obtained considering the nominal mass density: the process-induced porosity has a negligible influence on the dynamic properties of the material, as demonstrated by Kovacik [73].

The trend obtained as a function of the energy density is not altered by the solutioning and aging treatments (Fig. 7), confirming the absence of significant microstructural changes following the heat treatments (i.e., the adopted heat treatments preserve the features produced by the printing process) and a negligible influence of any process-induced residual stress, which are present in the as-built material conditions. This allows to discuss the effects of the microstructure on the dynamic behavior regardless of the heat treatment undergone by the material.

Excluding the effects of the specimen's actual geometry and mass density, the material's microstructure is the only element capable of justifying the dynamic Young modulus variations as a function of the process parameters. Also, the trend obtained as a function of the energy density is not altered by the solutioning and aging treatments (Fig. 7), confirming the absence of significant microstructural changes following the heat treatments (i.e., the adopted heat treatments preserved the microstructural features produced by the printing process) and a negligible influence of any process-induced residual stress, which are present in the as-built material conditions, thus allowing to consider only the aged microstructure. As the energy density decreases, the microstructure features cooling dendritic structures with progressively smaller dimensions and more randomly oriented with respect to the build direction (Fig. 12). Consequently, the material becomes more isotropic and similar to the Inconel 718 obtained through conventional production processes until a limit structure is reached at $E_d = 45.4$ J/mm^3, consistently with the trend obtained for the dynamic Young modulus (Fig. 7). Dynamically, the columnar structures could constitute a preferential direction for the propagation of elastic waves, which propagate at limited speeds (i.e., reduced dynamic Young modulus). On the other side, the microstructure obtained at lower energy density values does not have a preferential path for the propagation of elastic waves, which are reflected between the crystalline grains boundaries at higher speeds (i.e., higher dynamic Young modulus). Furthermore, the slight decrease of the dynamic Young modulus experienced for the A_5 and A_6 process parameters (approximately 1%) can be attributed to the marked reduction of the material density observed for those sets. In summary, it may be hypothesized that the dynamic Young modulus depends on the material's grain size and orientation following a trend similar to that obtained by varying the energy density and approximately parabolic:

$$\begin{cases} E = -0.1569E_d^2 + 13.34E_d - 88.06 & \text{As} - \text{built} \\ E = -0.1581E_d^2 + 13.34E_d - 79.50 & \text{Solutioned} \\ E = -0.1575E_d^2 + 13.32E_d - 77.29 & \text{Aged} \end{cases}$$

and increasing until reaching the finest (and more isotropic) material's microstructure ($E_d = 45.4$ J/mm^3). Then, if the energy density is further reduced, the microstructure is approximately unchanged, but the dynamic Young modulus undergoes a slight reduction due to the increase in the material porosity (Table 5).

6 Conclusions

In the present study, the influence of the process parameters and heat treatments on the dynamic behavior of specimens in Inconel 718 obtained by laser powder bed fusion (L-PBF) is investigated. The L-PBF process parameters were defined

using first-order analytical models to avoid lack of fusion or keyhole defects. Two dimensionless parameters were used to describe the feasible region of the process and choose the parameter combinations to be studied. Ping tests were used to identify the Young modulus and the structural damping of the material as a function of the energy density. The specimens were tested in as-built, solutioned, and aged conditions. After the execution of the ping tests, the material's microstructure of several specimens was investigated through low-magnification optical microscopy. The main features and conclusions of the proposed work are the following:

- While prior research primarily explored the influence of the strain rate on the material's behavior, the proposed investigation fills a critical gap in the current knowledge base and delves into the intricate dynamics of additively manufactured materials, with a specific emphasis on the dynamic Young modulus and structural damping obtained for several process parameters combinations and heat treatments. Moreover, a novel systematic methodology based on ping tests was proposed to assess the dynamic behavior of any additively manufactured material.
- The results show that the dynamic Young modulus increases as energy density decreases following a parabolic trend until reaching a plateau for $E_d = 45.4\,\mathrm{J/mm^3}$ (corresponding to a 23% increase compared to the *Baseline* parameters), whereas the structural damping is approximately constant and equal to $\zeta = 0.0009$ for all the analyzed test conditions.
- The dynamic Young modulus trend obtained in as-built conditions is preserved after the execution of the solutioning and aging heat treatments, which further increase the dynamic Young modulus. In other terms, any process-induced residual stress has a negligible influence on the dynamic behavior of the printed material.
- A significant microstructural variation was observed for the adopted process parameters. The main differences concern the direction of the cooling thermal gradient and the appearance of alternative solidification directions as the process energy density decreases. The *Baseline* parameters produce dendritic structures oriented along the build direction and with high longitudinal extension. On the other side, the lower energy density sets produce a more isotropic material and smaller grains. The microstructure variations were consistently correlated with the dynamic results.
- The research showed that the L-PBF process parameters can be fine-tuned to modify the material's dynamic Young modulus without altering its structural damping. This knowledge is essential for optimizing material properties, ensuring the reliability and performance of additively manufactured components, and aiding in their optimization for a wide range of applications in which mechanical parts are subject to vibrations of different magnitudes. As an example, the dynamic Young modulus variations observed may be fundamental for all the Inconel 718 applications in which it is necessary to shift the system's natural frequencies to avoid any intersection with its working regimes (extending the component's life and preventing the system's failure).

Author Contributions All the authors contributed to the study conceptualization, validation, writing, reviewing, and editing. Methodology, material and software preparation, investigation, data collection, and analysis were performed by Michele Abruzzo and Giuseppe Macoretta. The first draft of the manuscript was written by Michele Abruzzo, and all authors commented on previous versions of the manuscript. All authors read and approved the final manuscript.

Funding Open access funding provided by Università di Pisa within the CRUI-CARE Agreement. Financed by the European Union - NextGenerationEU (National Sustainable Mobility Center CN00000023, Italian Ministry of University and Research Decree n. 1033 - 17/06/2022, Spoke 11 - Innovative Materials & Lightweighting).

Declarations

Competing interests The authors declare no competing interests.

Disclaimer The opinions expressed are those of the authors only and should not be considered representative of the European Union or the European Commission's official position. Neither the European Union nor the European Commission can be held responsible for them.

References

1. Stavropoulos P, Foteinopoulos P, Papacharalampopoulos A, Bikas H (2018) Addressing the challenges for the industrial application of additive manufacturing: towards a hybrid solution. Int J Lightweight Mater Manuf 1(3):157–168. https://doi.org/10.1016/j.ijlmm.2018.07.002
2. Armstrong, M, Mehrabi H, Naveed N (2022) An overview of modern metal additive manufacturing technology. J Manuf Process 84:1001–1029. https://www.sciencedirect.com/science/article/pii/S1526612522007459. https://doi.org/10.1016/j.jmapro.2022.10.060

3. Frazier WE (2014) Metal additive manufacturing: a review. J Mater Eng Perform 23:19171928. https://doi.org/10.1007/s11665-014-0958-z
4. Jebaraj JJ, Morrison DJ, Suni II (2014) Hydrogen diffusion coefficients through Inconel 718 in different metallurgical conditions. Corros Sci 80:517–522. https://www.sciencedirect.com/science/article/pii/S0010938X13004848. https://doi.org/10.1016/j.corsci.2013.11.002
5. Macoretta G et al (2021) Hydrogen embrittlement in Inconel 718 produced by selective laser melting. https://doi.org/10.1115/PVP2021-60453. https://asmedigitalcollection.asme.org/PVP/proceedings-pdf/PVP2021/85338/V003T05A001/6781527/v003t05a001-pvp2021-60453.pdf
6. Echeta I, Feng X, Dutton B, Leach R, Piano S (2020) Review of defects in lattice structures manufactured by powder bed fusion. Int J Adv Manuf Technol 106:2649–2668. https://doi.org/10.1007/s00170-019-04753-4
7. du Plessis A et al (2019) Beautiful and functional: a review of biomimetic design in additive manufacturing. Addit Manuf 27:408–427. https://www.sciencedirect.com/science/article/pii/S2214860419302611. https://doi.org/10.1016/j.addma.2019.03.033
8. Benedetti M et al (2021) Architected cellular materials: a review on their mechanical properties towards fatigue-tolerant design and fabrication. Mater Sci Eng R 144:100606 (2021). https://www.sciencedirect.com/science/article/pii/S0927796X21000012. https://doi.org/10.1016/j.mser.2021.100606
9. Jam A et al (2022) Manufacturability of lattice structures fabricated by laser powder bed fusion: a novel biomedical application of the beta Ti-21S alloy. Addit Manuf 50:102556. https://www.sciencedirect.com/science/article/pii/S221486042100703X. https://doi.org/10.1016/j.addma.2021.102556
10. Zhang J et al (2022) Enhancing specific energy absorption of additively manufactured titanium lattice structures through simultaneous manipulation of architecture and constituent material. Addit Manuf 55:102887. https://www.sciencedirect.com/science/article/pii/S221486042200286X. https://doi.org/10.1016/j.addma.2022.102887
11. Sokollu B, Gulcan O, Konukseven EI (2022) Mechanical properties comparison of strut-based and triply periodic minimal surface lattice structures produced by electron beam melting. Addit Manuf 60:103199. https://www.sciencedirect.com/science/article/pii/S2214860422005887. https://doi.org/10.1016/j.addma.2022.103199
12. Zhang X et al (2022) Additive manufacturing of intricate lattice materials: ensuring robust strut additive continuity to realize the design potential. Addit Manuf 58:103022. https://www.sciencedirect.com/science/article/pii/S2214860422004146. https://doi.org/10.1016/j.addma.2022.103022
13. Rupal BS, Li X, Rajani HRZ, Chen Z, Qureshi AJ (2022) Porosity and shape deviation analysis of lattice structures manufactured using laser powder bed fusion process. Procedia CIRP 114:48–53. https://doi.org/10.1016/j.procir.2022.10.007
14. Hosseini E, Popovich V (2019) A review of mechanical properties of additively manufactured Inconel 718. Addit Manuf 30:100877. https://doi.org/10.1016/j.addma.2019.100877
15. Wu Z, Narra S, Rollett A (2020) Exploring the fabrication limits of thin-wall structures in a laser powder bed fusion process. Int J Adv Manuf Technol 110:191–207. https://doi.org/10.1007/s00170-020-05827-4
16. Cherry J et al (2015) Investigation into the effect of process parameters on microstructural and physical properties of 316L stainless steel parts by selective laser melting. Int J Adv Manuf Technol 76:869–879. https://doi.org/10.1007/s00170-014-6297-2
17. Song B, Dong S, Liao H, Coddet C (2012) Process parameter selection for selective laser melting of Ti6Al4V based on temperature distribution simulation and experimental sintering. Int J Adv Manuf Technol 61:967–974. https://doi.org/10.1007/s00170-011-3776-6
18. Sanchez S et al (2021) Powder bed fusion of nickel-based superalloys: a review. International Journal of Machine Tools and Manufacture 165. https://www.scopus.com/inward/record.uri?eid=2-s2.0-85105692435&doi=10.1016%2fj.ijmachtools.2021.103729&partnerID=40&md5=eca7709ff3ae0227cf94cb4a2549f2fc. https://doi.org/10.1016/j.ijmachtools.2021.103729, cited by: 134; All Open Access, Green Open Access, Hybrid Gold Open Access
19. Mojumder S, Gan Z, Li Y, Amin AA, Liu WK (2023) Linking process parameters with lack-of-fusion porosity for laser powder bed fusion metal additive manufacturing. Addit Manuf 68:103500. https://www.sciencedirect.com/science/article/pii/S2214860423001136. https://doi.org/10.1016/j.addma.2023.103500
20. Shahwaz, M, Nath, P, Sen, I (2022) A critical review on the microstructure and mechanical properties correlation of additively manufactured nickel-based superalloys.J Alloys Compd 907:164530. https://doi.org/10.1016/j.jallcom.2022.164530
21. Molinari A et al (2018) (2018) Mechanical properties of porous structures produced by selective laser melting of a Ti6Al4V alloy powder. Journal of the Japan Society of Powder and Powder Metallurgy 65(8):481–485. https://doi.org/10.2497/jjspm.65.481
22. Benedetti M et al (2019) Study of the compression behaviour of Ti6Al4V trabecular structures produced by additive laser manufacturing. Materials 12(9). https://www.mdpi.com/1996-1944/12/9/1471. https://doi.org/10.3390/ma12091471
23. Hyer HC, Petrie CM (2022) Effect of powder layer thickness on the microstructural development of additively manufactured SS316. J Manuf Process 76:666–674. https://www.sciencedirect.com/science/article/pii/S1526612522001463. https://doi.org/10.1016/j.jmapro.2022.02.047
24. Pimenov D et al (2023) Influence of selective laser melting process parameters on the surface integrity of difficult-to-cut alloys: comprehensive review and future prospects. Int J Adv Manuf Technol 127:1071–1102. https://doi.org/10.1007/s00170-023-11541-8
25. Moda M, Chiocca A, Macoretta G, Monelli BD, Bertini L (2022) Technological implications of the Rosenthal solution for a moving point heat source in steady state on a semi-infinite solid. Materials & Design 223:110991. https://doi.org/10.1016/j.matdes.2022.110991
26. Yim S, Bian H, Aoyagi K, Yamanaka K, Chiba A (2023) Effect of powder morphology on flowability and spreading behavior in powder bed fusion additive manufacturing process: a particle-scale modeling study. Addit Manuf 72:103612. https://www.sciencedirect.com/science/article/pii/S2214860423002257. https://doi.org/10.1016/j.addma.2023.103612
27. Olakanmi E (2013) Selective laser sintering/melting (SLS/SLM) of pure Al, Al-Mg, and Al-Si powders: effect of processing conditions and powder properties. J Mater Process Technol 213(8):1387–1405. https://doi.org/10.1016/j.jmatprotec.2013.03.009
28. Balbaa M et al (2021) Role of powder particle size on laser powder bed fusion processability of AlSi10Mg alloy. Addit Manuf 37:101630. https://www.sciencedirect.com/science/article/pii/S2214860420310022. https://doi.org/10.1016/j.addma.2020.101630
29. He C, Ramani KS, Okwudire CE (2023) An intelligent scanning strategy (SmartScan) for improved part quality in multi-laser PBF additive manufacturing. Addit Manuf 64:103427. https://www.sciencedirect.com/science/article/pii/S2214860423000404. https://doi.org/10.1016/j.addma.2023.103427
30. Zhao R et al (2022) On the role of volumetric energy density in the microstructure and mechanical properties of laser powder bed fusion Ti-6Al-4V alloy. Additive Manufacturing 51:102605. https://www.sciencedirect.com/science/article/

pii/S2214860422000136. https://doi.org/10.1016/j.addma.2022.102605
31. Zhang W, Tong M, Harrison NM (2020) Scanning strategies effect on temperature, residual stress and deformation by multi-laser beam powder bed fusion manufacturing. Addit Manuf 36:101507. https://www.sciencedirect.com/science/article/pii/S2214860420308794. https://doi.org/10.1016/j.addma.2020.101507
32. Calandri M et al (2019) Texture and microstructural features at different length scales in Inconel 718 produced by selective laser melting. Materials 12(8):1293. https://doi.org/10.3390/ma12081293
33. Guo S et al (2023) Microstructure and mechanical properties of Ti6Al4V/ B4C titanium matrix composite fabricated by selective laser melting (SLM). J Mater Res Technol 23:1934–1946. https://doi.org/10.1016/j.jmrt.2023.01.126
34. Liverani E, Toschi S, Ceschini L, Fortunato A (2017) Effect of selective laser melting (SLM) process parameters on microstructure and mechanical properties of 316L austenitic stainless steel. J Mater Process Technol 249:255–263. https://doi.org/10.1016/j.jmatprotec.2017.05.042
35. Trevisan F et al (2017) On the selective laser melting (SLM) of the AlSi10Mg alloy: process, microstructure, and mechanical properties. Materials 10(1):76. https://doi.org/10.3390/ma10010076
36. Facchini L et al (2010) Ductility of a Ti-6Al-4V alloy produced by selective laser melting of prealloyed powders. Rapid Prototyp J 16(6):450–459. https://doi.org/10.1108/13552541011083371
37. Ravichander BB, Amerinatanzi A, Moghaddam NS (2020) Study on the effect of powder-bed fusion process parameters on the quality of as-built IN718 parts using response surface methodology. Metals 10(9):1180. https://doi.org/10.3390/met10091180
38. Liu S, Li H, Qin C, Zong R, Fang X (2020) The effect of energy density on texture and mechanical anisotropy in selective laser melted Inconel 718. Materials & Design 191:108642. https://doi.org/10.1016/j.matdes.2020.108642
39. Wu H et al (2017) Effect of laser parameters on microstructure, metallurgical defects and property of AlSi10Mg printed by selective laser melting. J Micromech Mol Phys 02(04):1750017. https://doi.org/10.1142/s2424913017500175
40. Zhang H et al (2020) Microstructure and tribological property of selective laser melted Ni-based composites using different scanning strategies. Vacuum 177. https://doi.org/10.1016/j.vacuum.2020.109439
41. Simonelli M, Tse Y, Tuck C (2014) Effect of the build orientation on the mechanical properties and fracture modes of SLM Ti-6Al-4V. Adv Mater Sci Eng A 616:1–11. https://doi.org/10.1016/j.msea.2014.07.086
42. Bertolini R, Perini M, Ghiotti A, Bruschi S (2022) The effect of the building direction and surface finish on the mechanical properties of the direct energy deposited AISI 316L stainless steel. Manuf Lett 33:109–116. https://doi.org/10.1016/j.mfglet.2022.07.047
43. Ma X et al (2020) Fatigue short crack propagation behavior of selective laser melted Inconel 718 alloy by in-situ SEM study: influence of orientation and temperature. Int J Fatigue 139:105739. https://doi.org/10.1016/j.ijfatigue.2020.105739
44. Macoretta G, Bertini L, Monelli B, Berto F (2023) Productivity-oriented SLM process parameters effect on the fatigue strength of Inconel 718. Int J Fatigue 168:107384. https://doi.org/10.1016/j.ijfatigue.2022.107384
45. Nezhadfar P, Thompson S, Saharan A, Phan N, Shamsaei N (2021) Structural integrity of additively manufactured aluminum alloys: effects of build orientation on microstructure, porosity, and fatigue behavior. Addit Manuf 47:102292. https://www.sciencedirect.com/science/article/pii/S2214860421004528. https://doi.org/10.1016/j.addma.2021.102292
46. Isaac JP et al (2022) Role of build orientation on quasi-static and dynamic fracture responses of additively manufactured AlF357 and AlSi10Mg alloys. Addit Manuf 59:103080. https://www.sciencedirect.com/science/article/pii/S2214860422004705. https://doi.org/10.1016/j.addma.2022.103080
47. Birosz MT, Safranyik F, Andó M (2022) Build orientation optimization of additive manufactured parts for better mechanical performance by utilizing the principal stress directions. J Manuf Process 84:1094–1102. https://www.sciencedirect.com/science/article/pii/S1526612522007319. https://doi.org/10.1016/j.jmapro.2022.10.038
48. Gerstgrasser M, Cloots M, Stirnimann J, Wegener K (2021) Residual stress reduction of LPBF-processed CM247LC samples via multi laser beam strategies. Int J Adv Manuf Technol 117:2093–2103. https://doi.org/10.1007/s00170-021-07083-6
49. Balbaa M, Mekhiel S, Elbestawi M, McIsaac J (2020) On selective laser melting of Inconel 718: densification, surface roughness, and residual stresses. Materials & Design 193:108818. https://doi.org/10.1016/j.matdes.2020.108818
50. Ali H, Ghadbeigi H, Mumtaz K (2018) Processing parameter effects on residual stress and mechanical properties of selective laser melted Ti6Al4V. J Mater Eng Perform 27(8):4059–4068. https://doi.org/10.1007/s11665-018-3477-5
51. Wang X, Chou K (2019) The effects of stress relieving heat treatment on the microstructure and residual stress of Inconel 718 fabricated by laser metal powder bed fusion additive manufacturing process. J Manuf Process 48:154–163. https://www.sciencedirect.com/science/article/pii/S1526612519303676. https://doi.org/10.1016/j.jmapro.2019.10.027
52. Zou X et al (2022) Residual stress control of 316 L stainless steel using pulsed-wave laser additive manufacturing. Opt Laser Technol 150:107910. https://doi.org/10.1016/j.optlastec.2022.107910
53. Tucho WM, Cuvillier P, Sjolyst-Kverneland A, Hansen V (2017) Microstructure and hardness studies of Inconel 718 manufactured by selective laser melting before and after solution heat treatment. Mater Sci Eng A 689:220–232. https://doi.org/10.1016/j.msea.2017.02.062
54. Shin W-S et al (2021) Heat treatment effect on the microstructure, mechanical properties, and wear behaviors of stainless steel 316L prepared via selective laser melting. Mater Sci Eng A 806:140805. https://doi.org/10.1016/j.msea.2021.140805
55. Richetta M, Varone A (2020) A focus on dynamic modulus: effects of external and internal morphological features. Metals 11(1):40. https://doi.org/10.3390/met11010040
56. Chung DDL (2001) Review: materials for vibration damping. J Mater Sci 36(24):5733–5737. https://doi.org/10.1023/a:1012999616049
57. Maconachie T et al (2020) Effect of build orientation on the quasi-static and dynamic response of SLM AlSi10Mg. Mater Sci Eng A 788:139445. https://doi.org/10.1016/j.msea.2020.139445
58. Carassus H et al (2022) An experimental investigation into influences of build orientation and specimen thickness on quasi-static and dynamic mechanical responses of selective laser melting 316L stainless steel.Mater Sci Eng A 835:142683. https://doi.org/10.1016/j.msea.2022.142683
59. Ge Y, Lei J, Liu T, Bai W (2021) Dynamic mechanical properties and constitutive model of selective laser melting 316L stainless steel at different scanning speeds. Advances in Materials Science and Engineering. https://doi.org/10.21203/rs.3.rs-835137/v1
60. Scalzo F, Totis G, Sortino M (2022) Influence of the experimental setup on the damping properties of SLM lattice structures. Exp Mech 63(1):15–28. https://doi.org/10.1007/s11340-022-00898-8
61. Wang Y, Lu Y, Mendez PF (2019) Scaling expressions of characteristic values for a moving point heat source in steady state on a semi-infinite solid. Int J Heat Mass Transfer 135:1118–1129. https://doi.org/10.1016/j.ijheatmasstransfer.2019.02.042

62. Mendez PF, Lu Y, Wang Y (2018) Scaling analysis of a moving point heat source in steady-state on a semi-infinite solid. J Heat Transf 140(8). https://doi.org/10.1115/1.4039353
63. ASTM (2015) E1876 - dynamic Young's modulus, shear modulus, and Poisson's ratio by impulse excitation of vibration
64. Schindelin J et al (2012) Fiji: an open-source platform for biological-image analysis. Nat Methods 9(7):676–682. https://doi.org/10.1038/nmeth.2019
65. Tian Y et al (2014) Rationalization of microstructure heterogeneity in Inconel 718 builds made by the direct laser additive manufacturing process. Metall and Mater Trans A 45:4470–4483. https://doi.org/10.1007/s11661-014-2370-6
66. Huynh T et al (2022) Microstructural development in Inconel 718 nickel-based superalloy additively manufactured by laser powder bed fusion. Metallography, Microstructure, and Analysis 11. https://doi.org/10.1007/s13632-021-00811-0
67. Special metals (2007) Inconel alloy 718 - SMC-045
68. Soderstrom E, Mendez P (2006) Humping mechanisms present in high speed welding. Science and Technology of Welding and Joining 11(5):572–579. https://doi.org/10.1179/174329306X120787
69. Chowdhury S et al (2022) Laser powder bed fusion: a state-of-the-art review of the technology, materials, properties & defects, and numerical modelling. J Mater Res Technol 20:2109–2172. https://doi.org/10.1016/j.jmrt.2022.07.121
70. Huang L, Cao Y, Li G, Wang Y (2020) Microstructure characteristics and mechanical behaviour of a selective laser melted Inconel 718 alloy. J Mater Res Technol 9(2):2440–2454. https://doi.org/10.1016/j.jmrt.2019.12.075
71. Marchese G et al (2020) The influence of the process parameters on the densification and microstructure development of laser powder bed fused Inconel 939. Metals 10(7). https://www.mdpi.com/2075-4701/10/7/882. https://doi.org/10.3390/met10070882
72. Chirikov V, Dimitrov D, Boyadjiev Y (2020) Determination of the dynamic Young's modulus and Poisson's ratio based on higher frequencies of beam transverse vibration. Procedia Manufact 46:87–94. https://doi.org/10.1016/j.promfg.2020.03.014
73. Kováčik J (1999) Correlation between Young's modulus and porosity in porous materials. J Mater Sci Lett 18(13):1007–1010. https://doi.org/10.1023/a:1006669914946